The Influence of Size on the Intracranial Distribution of Biomedical Nanoparticles Administered by Convection-enhanced Delivery in Minipigs

Mahsa Amirrashedi,* Andreas Ingemann Jensen,*,◆ Qing Tang, Natan Johannes Willem Straathof, Katharina Ravn, Christian G.T. Pedersen, Louise Langhorn, Frantz Rom Poulsen, Max Woolley, David Johnson, Julia Williams, Charlotte Kidd, Helge Thisgaard,*,◆ and Bo Halle*,◆

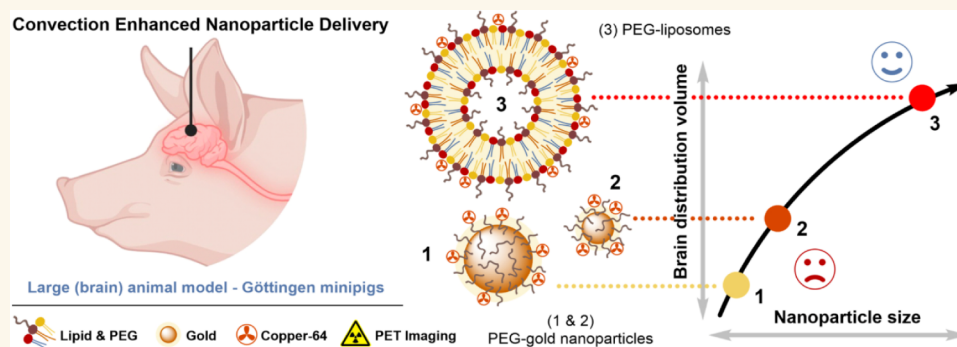**ABSTRACT:** Because of the blood−brain barrier (BBB), successful drug delivery to the brain has long been a key objective for the medical community, calling for pioneering technologies to overcome this challenge. Convection-enhanced delivery (CED), a form of direct intraparenchymal microinfusion, shows promise but requires optimal infusate design and real-time distribution monitoring. The size of the infused substances appears to be especially critical, with current knowledge being limited. Herein, we examined the intracranial administration of polyethylene glycol (PEG)-coated nanoparticles (NPs) of various sizes using CED in groups of healthy minipigs ($n = 3$). We employed stealth liposomes (LIPs, 130 nm) and two gold nanoparticle designs (AuNPs) of different diameters (8 and 40 nm). All were labeled with copper-64 for quantitative and real-time monitoring of the infusion via positron emission tomography (PET). NPs were infused via two catheters inserted bilaterally in the putaminal regions of the animals. Our results suggest CED with NPs holds promise for precise brain drug delivery, with larger LIPs exhibiting superior distribution volumes and intracranial retention over smaller AuNPs. PET imaging alongside CED enabled dynamic visualization of the process, target coverage, timely detection of suboptimal infusion, and quantification of distribution volumes and concentration gradients. These findings may augment the therapeutic efficacy of the delivery procedure while mitigating unwarranted side effects associated with nonvisually monitored delivery approaches. This is of vital importance, especially for chronic intermittent infusions through implanted catheters, as this information enables informed decisions for modulating targeted infusion volumes on a catheter-by-catheter, patient-by-patient basis.

continued...

INTRODUCTION

It is widely acknowledged that effective drug delivery to the brain is often hindered by the blood—brain barrier (BBB). This anatomical hurdle renders systemic drug administration futile against a vast spectrum of central nervous system (CNS) disorders and associated pathologies.[1] In severe medical conditions (*e.g.*, glioblastoma multiforme (GBM), diffuse intrinsic pontine glioma, and Parkinson's disease), direct administration of therapeutics into the affected regions of the brain, thereby bypassing the BBB, is highly desirable. One plausible remedy is to employ bulk convective flow at the infusion site, using so-called convection-enhanced delivery (CED). CED relies on the direct delivery of high drug concentrations using a hydrostatic pressure gradient generated through microcatheters implanted intracerebrally. Opposed to diffusion-driven strategies, CED allows for the expansive distribution of therapeutic agents within the brain parenchyma, reaching a larger volume of distribution and potentially covering more of the affected brain regions.[2,3]

The efficacy of CED is reliant upon several factors, chief among them being the optimal design and size of the infused species.[4−6] Small molecule therapeutic agents typically have short half-lives in the brain, leading to their swift elimination immediately after infusion.[7] This limitation can be addressed using nanoencapsulation, in this way artificially increasing the size of the administered compounds and protecting them from rapid clearance. Biomedically relevant nanoparticles (NPs) such as small gold nanoparticles (AuNPs),[8] polymeric micelles,[9,10] dendrimers,[11] and liposomes (LIPs)[12−14] minimize systemic toxicity, improve intracranial retention, and facilitate sustained release of their therapeutic cargo.[5] Once administered via CED, NPs must navigate through the brain's extracellular matrix (ECM). Their physiochemical properties, notably their size and surface architecture, are believed to play critical roles in determining their distribution within the brain. These properties are, therefore, central to aspects like penetration depth, distribution volume, and intracranial retention. As such, the size dependency of NPs on CED can be thought of as relating both to an initial distribution phase and a retention phase once the infusion has been terminated. Studies suggest that NPs exceeding diameters of 100 nm face challenges when moving through the brain's ECM, which typically displays openings of 38−64 nm in healthy tissue[15] and can fluctuate between 7 and 100 nm in tumor-affected areas.[16] As such, larger NPs would be expected to show limited distribution but increased retention within the brain, given that their size would hinder swift removal, whether through cellular absorption, glymphatic clearance, transit through perivascular routes, or clearance via capillaries. Conversely, smaller NPs might penetrate and distribute more extensively but might not remain in the tissue for as long. The small dimensions of such particles may accelerate their removal through clearance mechanisms or diffusive exits from the target. In this way, the dimension of NPs is likely to be a strategic variable that can be fine-tuned to optimize the effectiveness of NP delivery via CED, a topic that warrants deeper exploration. In addition to size, the surface architecture of the NPs is expected to be of key importance. Previous reports support that NPs with neutral or slightly negative surface charge (zeta potential) and coating with hydrophilic polymers such as polyethylene glycol (PEG) facilitate passage through the cerebral interstitium.[13] This is in line with established nanomedicine, in which such coatings are employed to limit the interaction of NPs with biological materials in the living organism.

In addition to delivering drugs, NPs can also serve as tracers during the infusion process.[17,18] This feature is of utmost importance in CED, which relies on precise and targeted infusion. By attaching suitable radionuclides to the NPs, the entire infusion process can be tracked and monitored non-invasively via nuclear imaging. This provides not only valuable real-time feedback on the effectiveness of the delivery method but also permits prompt identification of suboptimal infusion and enables optimizable modulation of infusion parameters. Despite the wealth of studies utilizing gadolinium (Gd)-enhanced magnetic resonance imaging (MRI) to characterize the distribution achieved via CED,[19−26] the potential of nuclear imaging modalities such as positron emission tomography (PET) remains largely untapped and has not yet been fully elucidated in the context of image-guided intracranial drug delivery. PET provides a sensitive alternative to MRI contrast for tracking and monitoring the spatiotemporal distribution of radiolabeled therapeutics during CED. Moreover, PET-guided delivery provides invaluable insight into the pharmacokinetics of the infused substance, including its dispersion, elimination, and clearance, adding an additional layer of quantitative information to the delivery process-.

Motivated by the promise of using NPs for drug delivery via CED and the need for optimized strategies for this, we here report an investigation of PET-guided intracranial CED of three different sizes of NPs (Figure 1). The central objective was to evaluate the impact of NP size on the two crucial delivery aspects of CED in the brain: volume of distribution (Vd) and intracranial retention. For the largest NP-type, we used LIPs with a volume-weighted hydrodynamic diameter ($\emptyset_{vol}$) of ~130 nm, LIP(130). LIPs are biocompatible and biodegradable lipid-based, spherical NPs, which can be readily manufactured by established methods with diameters of around 100 nm. In addition, LIPs can be readily labeled with PET radionuclides in the lipid bilayer membrane as well as in the inner aqueous compartment and used for *in vivo* PET imaging.[17,27] However, LIPs are challenging to prepare in small sizes. For this reason, we used AuNPs as models for the two smaller NP designs, with $\emptyset_{vol}$ of ~8 nm and ~40 nm, AuNP(8) and AuNP(40), respectively. AuNPs are biocompatible gold spheres that can be readily synthesized in tailored sizes in the 5−50 nm range using reported procedures.[18,28] We recently reported a practical method for surface labeling of AuNPs with radiometals for PET imaging, which was also used in the current study.[28] All three NP designs were coated with PEG (Figure 1), ensuring that their interaction with biological matter in the brain would be comparable, and were labeled with copper-64 (^{64}Cu-NPs), denominated as ^{64}Cu-AuNP (8), ^{64}Cu-AuNP (40), and ^{64}Cu-LIP (130), for quantitative PET imaging. We tested our delivery platform in pigs, driven by their anatomical brain similarities to humans. We used minipigs due to their slow growth rate, minimizing the risk of postimplantation catheter dislocation during the study. Concurrently, we employed clinical-grade
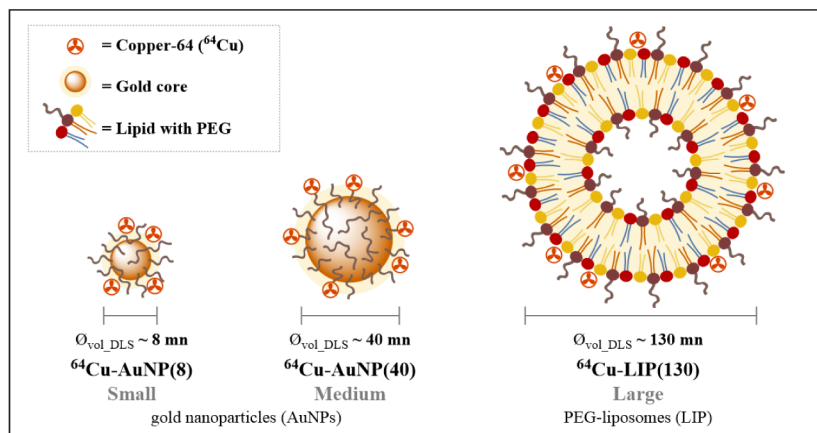
Figure 1. Graphical illustration of the different sizes of ^{64}Cu-NPs used in this study. For large NPs, we used LIPs with an average diameter of 130 nm, and for small and medium NPs, we used AuNPs with diameters of 8 and 40 nm, respectively. Abbreviations: NPs, nanoparticles; ^{64}Cu-NPs, radiolabeled nanoparticles with copper-64; AuNPs, gold nanoparticles; LIPs, liposomes; $\emptyset_{vol\text{-DLS}}$, the volume-weighted hydrodynamic diameter measured by dynamic light scattering.

Table 1. Properties of All Radiolabeled ^{64}Cu-NPs Administered Intracranially to Minipigs[a]

size classification	small	medium	large	large
$\emptyset_{vol\text{-DLS}}$ (nm), citrate-coated	5.4 ± 0.9	13.4 ± 0.8	n.a.	n.a.
$\emptyset_{vol\text{-DLS}}$ (nm), PEG-coated	7.5 ± 0.4	39.8 ± 6.9	134 ± 9	127 ± 10
$\emptyset_{UV/vis}$ (nm), PEG-coated	6.6 ± 0.6	68 ± 8	n.a.	n.a.
$\emptyset_{TEM}$ (nm)	4.8 ± 0.8	14.2 ± 1.3	n.a.	n.a.
PDI, PEG-coated	0.22 ± 0.01	0.15 ± 0.03	0.05 ± 0.01	0.13 ± 0.04
ζ pot. (mV), PEG-coated	−9.55	−4.86	−4.89	−2.45
number of NPs per mL	2.3×10^{13}	2.8×10^{11}	6.8×10^{12}	6.9×10^{12}
specific activity per NP (ndc.)	0.021 mBq/NP	1.73 mBq/NP	0.043 mBq/NP	0.067 mBq/NP
overall RCY (ndc.)	45%	43%	48%	45%
overall RCY (dc.)	56%	58%	55%	53%
NP name	^{64}Cu-AuNP(8)	^{64}Cu-AuNP(40)	^{64}Cu-LIP(130) (experiment #1)	^{64}Cu-LIP(130) (experiment #2)

[a]Reported data are given as mean ± standard deviation (n_{TEM} = 10, $nDLS$ = 5). Notes: ^{64}Cu-LIP(130) are synthesized and tested twice (experiments #1 and #2). The specific activity refers to the radioactivity for a single NP. The overall RCY refers to radiochemical yield (RCY) of the entire radiolabeling process. Abbreviations: $\emptyset_{vol\text{-DLS}}$, the volume-weighted hydrodynamic diameter measured by DLS; $\emptyset_{TEM}$, the diameter of the AuNP gold core measured by TEM; $\emptyset_{UV/Vis}$, the AuNP diameter corresponding to the absorption maximum according to ref[28]; PDI, polydispersity index; ζ, zeta potential; DLS, dynamic light scattering analysis; n.a., not applicable; TEM, transmission electron microscopy; UV/Vis, ultraviolet−visible spectroscopy; RCY, radiochemical yield; ndc., non-decay corrected; dc., decay corrected; RCC, radio chemical conversion.

CED devices to infuse ^{64}Cu-NPs into the minipig brain, a strategic choice made to uphold the relevance of the study by mimicking the conditions and challenges that would be encountered in actual clinical scenarios. By integrating clinical tools and large animal models within our experimental framework, we sought to enhance the reliability of our findings, thereby positioning our study at the forefront of translational research, where the insights and knowledge gained have the potential for direct implementation into the clinic.

RESULTS AND DISCUSSION

Synthesis and Characterization of Nanoparticles. To investigate the influence of NP size with CED, we prepared two different types of copper-64 labeled NPs (^{64}Cu-NPs) in three different sizes, small and medium AuNPs: ^{64}Cu-AuNP(8) and ^{64}Cu-AuNP(40), and large LIPs: ^{64}Cu-LIP(130) (Table 1). Small and medium AuNPs were synthesized as per previously published procedures.[28,29] In brief, copper-64 was bound to the AuNP surface using a conjugate of the macrocyclic chelator DOTA and 1,2-dithiolane, which exhibits a disulfide for stable attachment to metallic gold, followed by saturation with PEG. We previously reported excellent stability of this radiolabeling

strategy in both the cerebrospinal fluid and brain homogenate within the relevant study period.[28] Further, the chelate between DOTA and copper-64 is known to be highly stable *in vivo*, and is employed in clinically used radiotracers, such as DetectNet (Curium, ^{64}Cu-dotatate). The synthesis, radiolabeling, and characterization of the ^{64}Cu-NPs are detailed in Figures S1−S13 and Tables S1 and S2. Using different amounts of HAuCl$_4$, with and without tannic acid in a citrate buffer (pH = 7) yielded different sizes, small and medium, of citrate coated AuNPs, with $\emptyset_{vol\text{-DLS}}$ of 5.4 ± 0.9 nm and 13.4 ± 0.8 nm and polydispersity indices (PDIs) of 0.329 ± 0.011 and 0.319 ± 0.005, respectively, as judged by dynamic light scattering (DLS) analysis (Table 1). Next, the freshly prepared citrate-coated AuNPs were treated with ^{64}Cu-DOTA-TA. ^{64}Cu-DOTA-TA is a complex of [^{64}Cu]CuCl$_2$ in a DOTA (tetraxetan) chelator linked to a 1,2-dithiolane (2,2′,2′′-(10-(2-((2-(5-(1,2-dithiolan-3-yl)-pentanamido)ethyl)amino)-2-oxoethyl)-1,4,7,10 tetraazacyclo-dodecane-1,4,7-triyl) triacetic acid) moiety ("TA"). ^{64}Cu-DOTA-TA was obtained quantitively from complexing [^{64}Cu]-CuCl$_2$ with DOTA-TA with radiochemical conversion (RCC) of 96.8 ± 0.5% (n = 4). In all cases, both the medium and small AuNPs were successfully coated with the ^{64}Cu-DOTA-TA
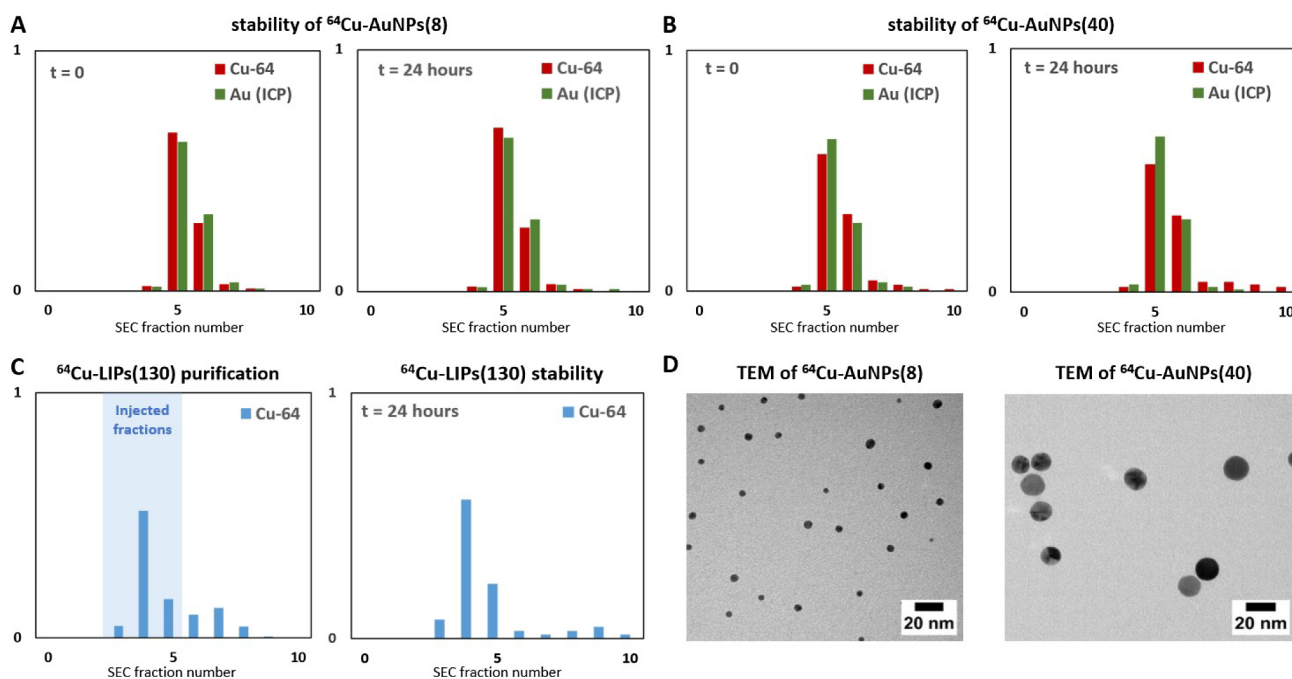
C

Figure 2. Analysis using SEC, ICP-OES, and TEM. Relative abundancy used on the *y*-axis, see Supporting Information for more details. (A) Analysis of ^{64}Cu-AuNP (8) stability on storage at room temperature, analyzed by SEC with quantification of ^{64}Cu by the dose calibrator and Au by ICP-OES. (B) Analysis of ^{64}Cu-AuNP (40) stability on storage at room temperature, analyzed by SEC with quantification of ^{64}Cu by the dose calibrator and Au by ICP-OES. (C) Purification of ^{64}Cu-LIP(130), with injected fractions highlighted (light blue box), followed by stability and integrity of ^{64}Cu-LIP(130) by SEC after 24 h. (D) TEM of ^{64}Cu-AuNP(8) and ^{64}Cu-AuNP(40). Abbreviations: SEC, size-exclusion chromatography; ICP-OES, inductively coupled plasma-optical emission spectrometry; TEM, transmission electron microscopy; ^{64}Cu-AuNP(8), radiolabeled gold nanoparticles with an average diameter of 8 nm; ^{64}Cu-AuNP(40), radiolabeled gold nanoparticles with an average diameter of 40 nm; ^{64}Cu-LIP(130), radiolabeled liposomes with an average diameter of 130 nm.

complex (RCC = 83.5 ± 9.4%, n = 4). The radiolabeled AuNPs were then treated with a final coating of MeO-PEG$_{2000}$-SH in sufficient excess to fully decorate the surface with PEG. It was observed that the coating procedure did not displace the already attached ^{64}Cu-DOTA-TA. The PEG-coated ^{64}Cu-AuNP were then reformulated by removal of the medium using a filtration filter, followed by redispersion in saline, then sterile-filtered, and characterized to give the final ^{64}Cu-AuNP dispersion, ^{64}Cu-AuNP(8) and ^{64}Cu-AuNP(40), ready for the *in vivo* studies in decay corrected (dc.) overall radiochemical yields (RCYs) of (57 ± 1%, n = 2) (Table 1 and S2). The small ^{64}Cu-AuNPs were measured by transmission electron microscopy (TEM) to be 4.8 ± 0.8 nm, and the medium-sized ones were measured to be 14.2 ± 1.3 nm (Table 1 and Figure 2D), which are in agreement with the initial seed size of the citrate-coated AuNPs as judged by DLS analysis earlier.

^{64}Cu-LIPs were prepared as the large NP-type in this study. After preparation, the ^{64}Cu-LIPs were purified by size exclusion chromatography (SEC) using a PD-10 column eluted with iso-HEPES buffer (pH = 7.4), followed by sterile filtration (0.45 μm) to give the final ^{64}Cu-LIP, ^{64}Cu-LIP(130), for the *in vivo* studies (374.5 ± 85.5 MBq, RCY = 54 ± 1% (dc.), n = 2) (Table 1 and S2).

The NPs prepared in this study were analyzed for gold (Au), or phosphorus (P) content by ICP-OES, relevant for AuNPs or LIPs, respectively. For the LIPs, the measured P content directly correlates to the phosphates of the phospholipids, which made it possible to calculate the number of NPs per milliliter.[30] For the AuNPs, the concentration of Au was used to calculate the number of AuNPs. The number of NPs was hypothesized to be of potential relevance to the ability of the administered NPs to

penetrate the brain tissue and not to saturate or clog available interstitial passageways. The NP preparations all contained a comparable number of NPs, in the range of 10^{11} to 10^{13} NPs per milliliter (Table 1). We also monitored the stability of the ^{64}Cu-NPs after 24 h, by analyzing *via* SEC after storage at room temperature (Figure 2A−C). This was done to ensure that the administered ^{64}Cu-NPs retained their integrity and did not lose the radiolabel. All prepared ^{64}Cu-NPs showed that only less than 1% of the ^{64}Cu activity was observed in the small molecular fractions (cutoff at fraction 7 and higher), suggesting excellent radiolabel stability after 24 h, and within the window of transportation and intracranial administration. The SEC stability analysis also depicted a clear overlap of the eluted ^{64}Cu activity, and the fractions containing the gold of the AuNPs, as judged by inductively coupled plasma-optical emission spectrometry (ICP-EOS) (Figure 2, brown versus green bars). It also shows the Au quantities per fraction, strongly suggesting that the ^{64}Cu-radiolabel remained associated with the AuNPs in both produced ^{64}Cu-AuNP (8) and ^{64}Cu-AuNP(40) (Figure 2A,B, respectively), demonstrating high stability of the NPs. A similar stability assay was also carried out for the liposomal NPs, with the relevant fractions containing ^{64}Cu-LIP(130) highlighted (Figure 2C, blue bars, light blue highlight). No noteworthy degradation of the ^{64}Cu-LIP(130) was observed after 24 h storage at room temperature, strongly indicating excellent radiolabel stability.

CED of Radiolabeled Nanoparticles in the Minipig Brain. The CED administration of ^{64}Cu-NPs was well-tolerated by all subjects. No adverse reactions to the NPs or neurological sequelae were noted following the surgical procedure or during infusion. No reflux or leakage was observed during infusion. It is
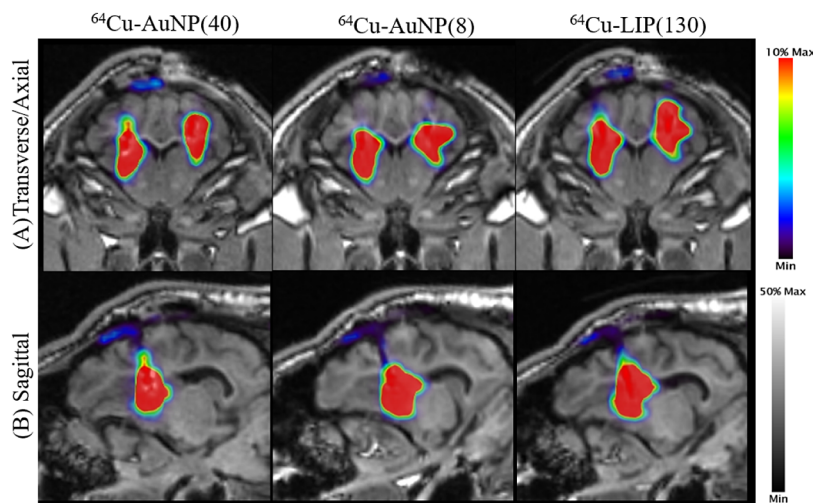
Figure 3. PET/MRI scans of the minipig brain post ^{64}Cu-NP infusion *via* CED. Representative PET/MRI scans of a minipig brain received ^{64}Cu-AuNP(40), ^{64}Cu-AuNP(8), and ^{64}Cu-LIP(130) upon completion of 2 hour infusion from (A) transverse and (B) sagittal views. Administration of ^{64}Cu-NPs was performed through two catheters implanted bilaterally within the putaminal regions. Abbreviations: NPs, nanoparticles; CED, convection-enhanced delivery; PET, positron emission tomography; MRI, magnetic resonance imaging; ^{64}Cu-AuNP(8), radiolabeled gold nanoparticles with an average diameter of 8 nm; ^{64}Cu-AuNP(40), radiolabeled gold nanoparticles with an average diameter of 40 nm; ^{64}Cu-LIP(130), radiolabeled liposomes with an average diameter of 130 nm.

noteworthy to mention that the ^{64}Cu-AuNP(8) and ^{64}Cu-AuNP(40) were examined in all subjects (n = 3). However, due to insufficient removal of the subcutaneous tissue in relation to the bone-anchored port in one subject, attachment of the application set was impossible after the initial infusion. This subject was thus excluded from the remainder of the study. To ensure sufficient sample size in each group of NPs and guarantee the statistical robustness of our findings, we repeated the ^{64}Cu-LIP(130) infusion twice in the remaining subjects (n = 4). The intermittent infusion performance of the neuroinfuse chronic drug delivery catheters (Renishaw Neuro Solutions Ltd., Wotton-Under-Edge, Gloucestershire, UK; Figure S14) remained unchanged during the whole study period, with no signs of intraparenchymal or subcutaneous infection, underlining the robustness of the chronic infusion device.

Sagittal and transverse PET/MRIs of a representative minipig brain illustrating the distribution of three distinct NPs following 120 min CED infusion are shown in Figure 3. The administered ^{64}Cu-NPs were easily distinguishable as a region of high signal intensity in the acquired PET images. Detailed presentation of dynamic PET frames and real-time tracking of ^{64}Cu-NPs infusions can be found in Figure S15–S17. During the infusion of all three types of ^{64}Cu-NPs, the Vd demonstrated a gradual increase in size over time without reaching a steady state even after a 120 min infusion.

As illustrated in Figures 3 and S15–S17, ^{64}Cu-LIP(130) exhibited a broader distribution than those achieved with the AuNPs and covered a more significant portion of the brain from both sagittal and transverse views. Moreover, medium-sized ^{64}Cu-AuNP(40) penetrated less than small-sized ^{64}Cu-AuNP-(8). The results of our observations aligned with the line profile outcomes in Figures 4A,B and S18, showing that ^{64}Cu-AuNP(40) remained more localized at the infusion site, while interestingly, LIPs and small AuNPs were observed to distribute outward more readily. The mean FWHM/FWTM was 8.7 ± 0.8/16 ± 1.5 mm for ^{64}Cu-LIP(130), 8.1 ± 0.05/14.8 ± 0.1 mm for ^{64}Cu-AuNP(8), and 7.01 ± 0.5/12.8 ± 1 mm for ^{64}Cu-AuNP(40) at T = 120 min (indicating the time when the

infusion was completed). While the difference was not deemed statistically significant, the area under the FWHM/FWTM plots (AUC) indicated that ^{64}Cu-LIP(130) had a greater distribution radius and penetration capacity than the AuNPs. Mean (AUC$_{FWHM}$/AUC$_{FWTM}$) was achieved for ^{64}Cu-LIP(130), yielding around 795.8 ± 42.4/1450.5 ± 77.2 mm·min, while the corresponding values were 759.6 ± 24/1384 ± 44 mm·min for ^{64}Cu-AuNP(8) and 684.1 ± 52.5/1247 ± 96 mm·min in the case of ^{64}Cu-AuNP(40).

We also assessed isocontours for a single catheter infused with different NPs to explore directional bias in the distribution cloud generated following infusion. As depicted in Figure 4C, iso-lines elicited slightly anisotropic dispersion of NPs, which attributed to both intrinsic properties of the infused NPs and the intricate architecture of the targeted region. Brain parenchyma is notorious for its heterogeneous cellular density, extracellular space, uneven portion of white/gray matter, and tissue elasticity across various regions. These differences contribute to a slightly nonuniform distribution of the infusate around the cannula tip, even in healthy brain tissue.[31]

Vd values attained by varying levels of threshold ranging from 10% to 90% at T = 120 min (the time point when the infusion was completed) are summarized in Figure 5A. As illustrated, the minimum volume of the brain exposed to at least 10% of the maximum obtained activity concentrations were calculated to be 2260 ± 111 μL for ^{64}Cu-LIP(130), 1321 ± 59 μL for ^{64}Cu-AuNP(8), and 763.5 ± 141 μL for [64]Cu--AuNP(40), which resulted in Vd$_{10\%}$ to volume of infusion (V_i) ratios of 3.9 ± 0.2 for ^{64}Cu-LIP(130), 2.9 ± 0.3 for ^{64}Cu-AuNP(8), and 2.1 ± 0.2 for ^{64}Cu-AuNP(40). Considering different threshold levels, the Vd values for ^{64}Cu-LIP(130) were 3.1 ± 0.1 and 2.2 ± 0.1 times greater than those for ^{64}Cu-AuNP(8) and ^{64}Cu-AuNP(40), respectively. These findings clearly demonstrate the superior -performance of ^{64}Cu-LIP(130) compared to the ^{64}Cu-AuNPs regarding distribution and penetration within the surrounding structure.

To further confirm our findings, we measured Vd at different time points for the above-mentioned thresholds and compared
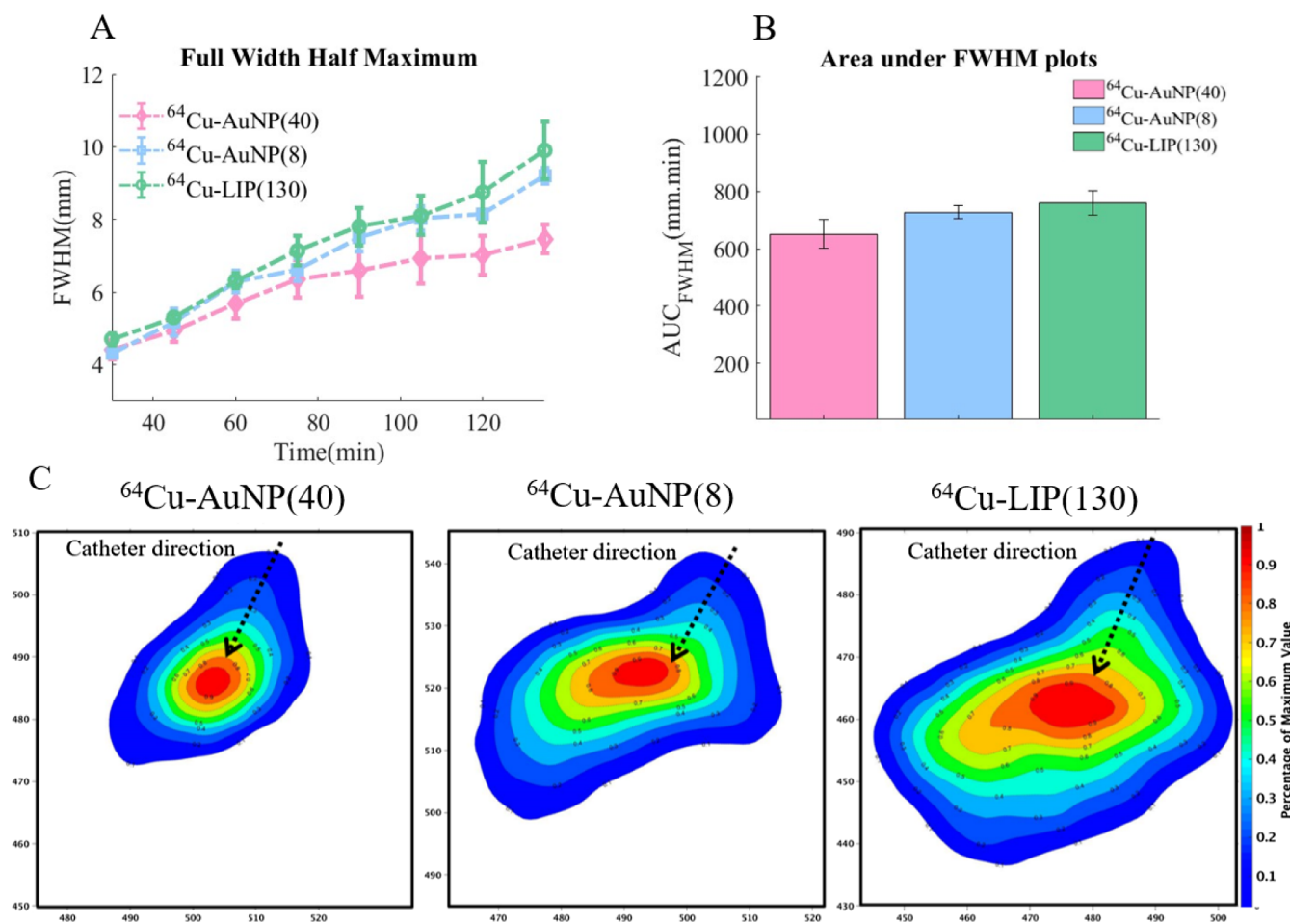
Figure 4. Line profile and iso-contour analysis for different ^{64}Cu-NPs. (A) Dynamic FWHM analysis of line profiles crossing the center of the catheter after infusion with different types of ^{64}Cu-NPs. (B) Corresponding AUC for FWHM plots. (C) Iso-contours for a single catheter (the same animal) infused with different ^{64}Cu-NPs at the end of a 120-min infusion. The process involved averaging three consecutive slices (including the catheter-visible target slice and two adjacent slices), normalizing to the maximum value, resampling to a finer sample size with a pixel size of 0.29 mm × 0.29 mm, and generating iso-contours. Pixels receiving the same percentage of infusion activity are shown with the same color (*e.g.*, an area with 0.5−0.6 of the maximum value is shown in green). Areas receiving <0.1 maximum value are masked out and shown in white. Black arrows indicate the approximate catheter direction. Abbreviations: FWHM, full-width half-maximum; AUC$_{FWHM}$, area under FWHM curves; ^{64}Cu-AuNP(8), radiolabeled gold nanoparticles with an average diameter of 8 nm; ^{64}Cu-AuNP(40), radiolabeled gold nanoparticles with an average diameter of 40 nm; ^{64}Cu-LIP(130), radiolabeled liposomes with an average diameter of 130 nm. Data are represented as mean $\pm$ standard error of the mean (n = 3−4).

the corresponding area under curve (AUC) values among NPs. Dynamically assessed Vd$_{10\%}$ and AUC$_{10\%}$ plots are illustrated in Figure 5B,C. Detailed analysis for other thresholds is also presented in Figure S19. The statistical comparison of Vd values and AUCs disclosed a meaningful difference for threshold levels of 10% up to 50% ($p < 0.05$). However, this discrepancy was not significant when we compared higher thresholds (>50%) among NPs, which primarily represent the regions located close to the catheter tip.

Normalized time activity curves (TACs) and related AUC values are presented in Figure 5D,E and S20. Briefly, the AUCs of normalized TAC were calculated as 26.3 ± 1.4, 39.3 ± 1.2, and 53.1 ± 4.1 for ^{64}Cu-AuNP(40), ^{64}Cu-AuNP(8), and ^{64}Cu-LIP(130), respectively. Specifically, ^{64}Cu-LIP(130) displayed a significantly higher retention than both types of AuNPs. The slight difference between ^{64}Cu-AuNP(8) and ^{64}Cu-AuNP(40) also hints at the potential influence of NP size on retention.

General Discussion. Current drug delivery strategies to the brain predominantly revolve around crossing the BBB. In addition, in the case of brain tumors, current efforts exploit the

compromised endothelial cell walls of the blood vessels in the blood−tumor barrier (BTB). Such strategies employ systemic administration, which has the immediate advantages of practical intravenous or even oral administration. For NPs, however, crossing the BBB has generally been of limited success, and while uptake in established tumors across the BTB can be achieved, this does not enable the targeting of cancer cells that have infiltrated further away from the tumor bulk, such as in GBM. For this reason, locoregional strategies for reaching such cancer cells, such as CED, are relevant.

Ongoing studies are unraveling the potential of NPs administered *via* CED, which were loaded with a combination of cargo and imaging probes.[10,12,14,32−36] To ensure efficient transport of NP-encapsulated agents using CED, several key properties have been highlighted;[5] For example, NPs must seemingly possess a size smaller than 100 nm to effectively navigate the ECM. Further, to minimize the likelihood of nonspecific binding to negatively charged components in the brain parenchyma, and enable wide distribution, the surface charge should be neutral or negatively charged.[13] Of particular
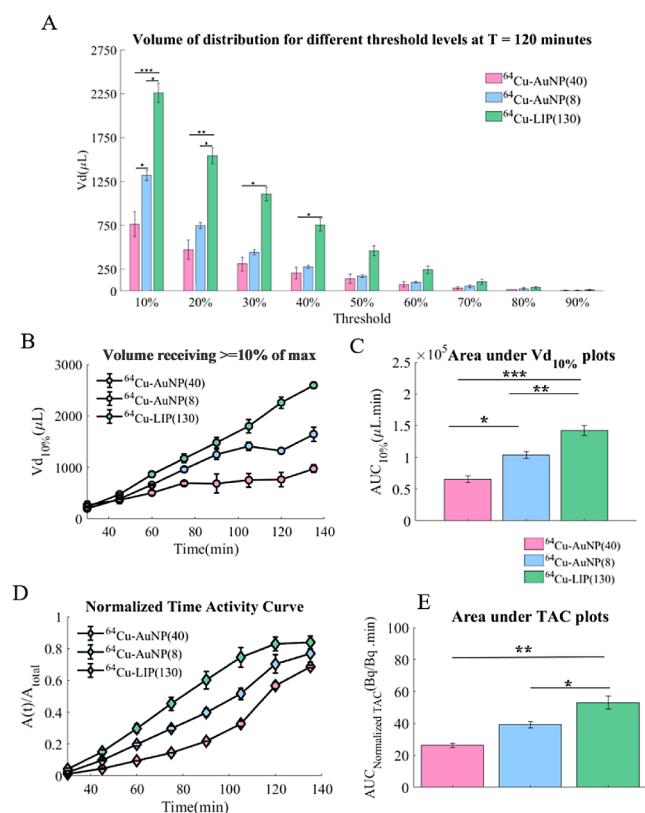
Figure 5. Vd, TAC, and corresponding AUC analysis for different ^{64}Cu-NPs. (A) Vd calculated for all ^{64}Cu-NPs using different threshold levels (10−90%) at the end of infusion (single time point). (B) Dynamic assessment of Vd for all -^{64}Cu-NPs using a 10% threshold and (C) corresponding AUCs for Vd$_{10\%}$ plots. (D) Normalized TAC plots to total injected activity administered to the whole brain VOI and (E) corresponding AUCs for all TAC plots. Abbreviations: Vd, volume of distribution; Vd$_{10\%}$, volume of distribution calculated with a threshold of 10%; ^{64}Cu-NPs, radiolabeled nanoparticles with copper-64; AUC, area under the curve; A(t), activity at a specific time point of t; A_{total}, total infused activity; TAC, time activity curve; VOI, volume of interest; ^{64}Cu-AuNP(8), radiolabeled gold nanoparticles with an average diameter of 8 nm; ^{64}Cu-AuNP(40), radiolabeled gold nanoparticles with an average diameter of 40 nm; ^{64}Cu-LIP(130), radiolabeled liposomes with an average diameter of 130 nm. Data are represented as mean ± standard error of the mean (n = 3−4). The significant difference was defined as *$p < 0.05$, **$p < 0.01$, and ***$p < 0.001$.

interest is the observation that cationic liposomes, with a binding constant 50 times higher for normal brain tissue, have a tissue distribution distance of approximately 3.5 times less than their neutral or negatively charged counterparts.[13,37,38] Surface coating made of PEG or dextran has been shown to minimize the rate of NP binding to brain cells during CED.[13,39]

With these properties in mind, we investigated the distribution of stealth LIPs and AuNPs in a range of sizes, by CED in a minipig model. NPs were synthesized in three sizes of small AuNPs (∼8 nm), medium AuNPs (∼40 nm), and large LIPs (∼130 nm), all radiolabeled with ^{64}Cu, enabling their monitoring through PET imaging. To quantify the distribution of NPs within the brain, we performed a comprehensive analysis of the acquired PET scans in terms of line profiles, iso-contours, and Vds of different thresholds. We also studied the retention properties of our NPs using TAC plots.

Based on our line profile analysis, all ^{64}Cu-NPs could distribute effectively within clinically relevant distances when administrated *via* CED using the neuroinfuse catheter and the chronic drug delivery system. As mentioned in similar reports, this is particularly important in GBM, which tends to recur within <2 cm from the initial tumor site.[36,40] The FWTM profiles crossing the catheter tip (without considering the partial volume effect) were observed to expand up to approximately 1.36 cm for ^{64}Cu-AuNP(40), and around 1.8 cm for ^{64}Cu-AuNP(8) and ^{64}Cu-LIP(130). Moreover, none of the ^{64}Cu-NPs reached a state of equilibrium, known as a steady state, even after the full 120 min infusion time. This observation suggests that by longer infusion times and increased volume of infusions or the number of catheters, it may be possible to reach even greater distances of ^{64}Cu-NP penetration in larger human brains, which should be the subject of further studies.

The Vd/V$_i$ in our study aligned well with those documented for NPs of approximately similar sizes in pigs[36] and small animal models.[41,42] However, slight differences in Vd/V$_i$ across different studies could be explained by several factors, including the characteristics of the NPs used, the presence or absence of a tumor environment, and the infusion parameters. The intrinsic properties of the NPs, such as their size, composition, shape, or surface chemistry, appear to significantly dictate their distribution within the brain. In addition, neuroinfuse catheter infusion optimization features and the parameters chosen during infusion, such as flow rate or duration, affect the distribution of the NPs. Furthermore, the methodologies applied in different studies, especially in image analysis and the thresholding techniques used to compute Vd values, contribute substantially to the observed discrepancies. Herein, we relied on Vd$_{10\%}$ as the primary threshold level to determine Vd/V$_i$. We also provided Vd values for other thresholds to gain a better understanding of the brain tissue exposed to different concentrations of ^{64}Cu-NPs, which is crucial for assessing the potential effectiveness of infused therapeutics in brain-targeted therapies. The statistical comparison of Vd and AUCs showed a significant difference for threshold levels of 10% to 50%. However, relatively higher thresholds (>50%) did not exhibit a significant difference for ^{64}Cu-NPs near the catheter tip. These findings may imply that while in the vicinity of the cannula, the infusion parameters play a pivotal role in the infusate reaching a greater distance, the impact of the NP-type and its properties on the Vd becomes more prominent as it convects further away from the administration site and encounters various anatomical and histological features that impede its distribution.

In our study, ^{64}Cu-AuNP administered by CED displayed a size-dependent diffusion and retention profile. We observed that smaller-sized ^{64}Cu-AuNP(8) navigated the brain's ECM more efficiently and reached a larger volume of distribution than ^{64}Cu-AuNP(40). However, the ECM, with its dense meshwork of glycoproteins and proteoglycans, can pose significant barriers to the diffusion of larger ^{64}Cu-AuNP(40). Moreover, ^{64}Cu-AuNP(8) also exhibited a slightly elevated retention compared to ^{64}Cu-AuNP(40), but the significance and quantitative effect of this on overall distribution is uncertain. Accordingly, and albeit speculative, we attribute the wider distribution of ^{64}Cu-AuNP(8) to a more favorable balance between distribution and retention from smaller NPs. However, the larger ^{64}Cu-LIP(130) significantly outperformed the two ^{64}Cu-AuNPs, in terms of both the distribution range and retention. In light of the discussion above, we attribute this especially to a very favorable retention of the larger NPs.

While size is clearly an important factor in NP distribution, the deformability and composition of LIPs give them a distinct possible advantage over AuNPs. LIPs are flexible, allowing them to maneuver through tight spaces more easily than the rigid AuNPs. It is plausible that this ability could become even more advantageous under the pressures of CED, where LIPs can potentially squeeze through more constricted areas. Second, there is a difference in density; while AuNPs are dense due to their gold core, LIPs are water-like in density. This lighter composition could allow them to move more freely within the tissue. Moreover, the small size of the AuNPs means that the random movements caused by Brownian motion become more dominant. Future studies should elucidate if density is a key factor in distribution by CED. It should be noted here that AuNPs in our study were used purely as a surrogate for NPs of a given size, as we believe biodegradable NP designs are more attractive for intracranial delivery.

Image-guided delivery enables real-time evaluation of drug distribution within the designated anatomical location and monitoring of the entire CED process. By far, Gd-based MRI stands out as the prevailing technique to characterize the delivery volumes attained through CED.[20,43,44] The European Medical Agency's restrictions on the use of linear Gd-based contrast agents after safety concerns, based on observations of Gd deposition in the brain, together with reported inaccuracies of imaging infusion volumes using T2/Flair,[45] highlight the challenges in monitoring the performance of intraparenchymal CED infusions using Gd-based MRI techniques. Moreover, MRI offers only an approximate visualization of the distribution, as it lacks precise quantitative data on the actual concentration of the infused compounds, which is another important aspect of interest in clinical applications. In contrast, PET presents a highly sensitive alternative to MRI for tracking and monitoring the distribution and concentration of radiolabeled therapeutics during CED. Coupling PET imaging with CED gives researchers the opportunity to acquire profound insights regarding the pharmacokinetics of the infused agents. Our study exemplified the capability of PET imaging by tracking the journey of our NPs inside the brain parenchyma, achieved through radiolabeling NPs with copper-64 using methods that have previously been shown to be stable *in vivo* for up to 3 h time frame, used in this study. Copper-64 boasts favorable decay properties with a half-life of 12.7 h and β+ emissions of $E_{max} = 0.653$ MeV,[46,47] making it a workhorse in NP imaging. Thanks to its coordination chemistry, copper-64 can be effectively conjugated to a wide range of biologically relevant molecules *via* chelation by DOTA, the macrocyclic chelator that was employed in our studies. While some studies have suggested a slight instability *in vivo* of the ^{64}Cu-DOTA chelate after intravenous administration, this chelator remains a widely used and very practical way of labeling with copper-64 for quantitative PET, both in research and in the clinic.

The present study is not without its limitations as it primarily focused on investigating the NP distribution in nontumor bearing minipigs, and thus, distribution properties are not entirely applicable to a tumorous milieu. Brain tumors like GBM are marked by a heterogeneous landscape, characterized by varying cellular compositions, necrotic zones, hemorrhage, and distinct growth dynamics. Consequently, different regions within the tumor may exhibit varying capabilities for penetration and distribution of NPs administered directly into tumoral zones. In an interesting study, it has been shown that even though V_d/V_i remains relatively consistent among normal and diverse tumor types, the intratumoral distribution of NPs is heterogeneous with a great tendency to accumulate in peritumoral space.[42] This distributional pattern can be attributed to both the intratumoral heterogeneity and elevated interstitial pressure stemming from increased vascular permeability and rapid tumor cell growth.[5] The increased pressure within the tumor creates resistance to the infused drug, presenting challenges in achieving reflux-free infusion and uniform drug penetration throughout the tumor mass.[48,49] Our iso-contour evaluation also highlighted that the distribution of ^{64}Cu-NPs is not entirely homogeneous. The NP type, infusion settings, possible heterogeneities in cellular density, and permeability across various brain tissues contribute to a slightly nonuniform and asymmetric distribution of the infused substance, a scenario that holds true even in healthy and nontumoral brain tissues. While these findings are instrumental, they still require exploration within tumoral conditions, to elucidate the potential implications for clinical applications. In the clinic, both resected and nonresected cases are to be treated. In tumor resected cases, the resection cavity poses a challenge in relation to catheter implantation, drug distribution around the entire cavity, and potential leakage into the cavity. Thus, large animal studies in tumor-bearing as well as tumor resected specimens are needed. Such studies should be conducted with chronic drug delivery systems such as neuroinfuse to successfully translate CED therapies into the clinic.

As previously mentioned, the properties of the targeted tissue and the type of NPs are just a few of the numerous factors that influence the ^{64}Cu-NPs distribution within the tissue. It is essential to acknowledge that flow dynamics of the infused NPs such as infusion rate/pressure and catheter design (size/type/length/shape/direction) used in the study are equally critical in determining the eventual dispersion pattern.[50−53] Herein, we employed a standardized infusion protocol, which, while suitable for controlled investigations, may not fully account for the dynamic and patient-specific nature of ^{64}Cu-NP delivery as encountered in real clinical settings. Individual patients may require tailored infusion parameters (*e.g.*, prolonged infusion times, increased number of catheters) based on their specific condition, tumor location, and its characteristics. Considering these complexities is imperative when designing and optimizing intracranial drug delivery strategies using CED techniques.[54]

In addition to delivery methods, the integration of radiolabeled NPs with PET/MRI offers advantages but may have limitations in CED studies, especially concerning safety considerations with nonendogenous and radioactive materials. Inorganic NPs may be a cause of inflammation in certain tissues.[55] However, gold is generally considered a biocompatible and nontoxic material,[56] although some studies have suggested the toxicity of AuNPs, especially at high concentrations.[57,58] To the best of our knowledge, no previous studies have found evidence of inflammation from direct intracranial administration of AuNPs. Our study did not thoroughly assess inflammation originating from the NP administration, but during the study period, no adverse effects were observed. The AuNPs were administered in relatively low amounts, at 0.12−0.18 mg/mL, and infusions were done for 2 hours, limiting concerns for acute inflammation. Most important, AuNPs were used here as model NPs for sizes and are not intended for clinical use. Another essential safety aspect pertains to radiation exposure. Despite administering small activities ranging from 20.81 to 42.63 Mbq in the current study, safety concerns regarding radiation exposure should always be considered. Other challenges such

as the limited scanner availability of PET/MRI scanners compared to PET/CT and ensuring compatibility of infusion devices with the imaging scanners to avoid potential artifacts and inaccuracies in quantification are additional noteworthy considerations. All in all, our findings support the potential of integrating ^{64}Cu-NPs and localized delivery methodologies as a promising therapeutic platform for addressing CNS-related disorders. However, before this approach can be translated into clinical practice, more in-depth investigations should be conducted to verify its reliability and robustness. Moreover, clinical implementation would require additional studies to optimize multiple attributes in relation to the NP design such as size, shape, surface properties, and cargo loading capacity, in order to enhance their ability to penetrate greater distances effectively. Furthermore, this study focused on exploring the size-dependent distribution of NPs administered *via* CED, and comparing these findings with the distribution observed in the absence of NPs could provide valuable insights and is an area worthy of further investigation.

CONCLUSIONS

In this study, we conducted a PET- guided intracranial CED of three differently sized ^{64}Cu-labeled NPs, ranging in diameters from 8 to 130 nm, *in vivo* in minipigs. Our results showcase the promising combination of CED and NPs for intracranial drug delivery and elucidate the impact of NP size on the distribution volume and brain retention. The comprehensive analysis of PET imaging data revealed substantial advantages for the larger liposomes (LIPs) over smaller gold nanoparticles (AuNP), evident in distribution volumes, penetration distance, and intracranial retention. Moreover, we observed slightly reduced penetration and retention of medium-sized ^{64}Cu-AuNP(40) compared to small-sized ^{64}Cu-AuNP(8). These findings support that larger NPs, around 100−150 nm, perform better in intracranial administration by CED and highlight the crucial role of NP size and physicochemical properties in this application. By employing a chronic CED system, designed specifically for use in long-term, intermittent, intraparenchymal infusions, we have in addition demonstrated feasibility for the translation of such a device for clinical evaluation.

EXPERIMENTAL SECTION

Animals and Housing. Three Göttingen female minipigs (Ellegaard Göttingen Minipigs A/S, Dalmose, Denmark) with an average weight of 9.3 ± 0.18 kg and approximately 2 months old were included in the present study. Minipigs were used due to their slow growth rate, making them optimal for long-term CED studies. All animal procedures were conducted per the approval from the Danish Animal Experiments Inspectorate (license no. 2020−15−0201−00553). The experiments were conducted according to the EU directive 2010/63/EU on the protection of animals used for scientific purposes. Detailed information regarding animals, housing, and perioperative procedures can be found in the Supporting Information.

Head Immobilization and Precatheter Implantation MRI. A dedicated MRI-compatible head frame (Renishaw Neuro Solutions Ltd., Wotton-Under-Edge, Gloucestershire, UK)[59,60] was used to fully immobilize the head before transferring the anesthetized animal to the scanner bed for preoperative MRI. All imaging was performed in a prone position using GE SIGNA 3T PET/MRI (GE Healthcare, Waukesha, WI, USA). The step-by-step overview of all

procedures involved on the surgery day is summarized in (Figure S21). 3D MRI scans of T1-weighted BRAVO and T2-weighted sequences were obtained using the upper anterior array (UAA). The preoperative MRI scans were then loaded into the neurosurgical planning software neuroinspire (Renishaw Neuro Solutions Ltd., Wotton-under-Edge, Gloucestershire, UK) to plan the implantation trajectories of two neuroinfuse CED catheters within the putaminal targets connected to an implanted transcutaneous port (Renishaw Neuro Solutions Ltd., Wotton-Under-Edge, Gloucestershire, UK), as illustrated in Figure S14A. To enable CED, the neuroinfuse chronic drug delivery system[61] and preclinical stereotactic system, developed by Renishaw Neuro Solutions Ltd., were utilized. Information regarding imaging protocols, devices, implantation of the neuroinfuse system, and postoperative recovery of the animals is detailed in Supporting Information.

Infusion Method of Radiolabeled Nanoparticles (^{64}Cu-NPs). The administration of ^{64}Cu-NPs commenced 7 days after catheter implantation by connecting the application set to the transcutaneous port (Figures S21B and 14C). Infusions were repeated through the transcutaneous port at weekly intervals for 4 weeks. Each week, a different type of ^{64}Cu-NPs was synthesized (as described in Supporting Information) and infused into the subjects. The infusion method of ^{64}Cu-NPs is shown in Figure S21B. Briefly, two 300 μL fixed volume extension sets (FVES) were filled with dispersions of radio-labeled NPs at specific sizes for each infusion. One end of the FVES tube was connected to the corresponding delivery channel of the 4-channel port application set (only 2/4 port channels were accessed for this study), while the other end was attached to a 6 m extension line, which in turn connected to standard syringes prefilled with artificial CSF (Figure S21B). The extension lines were utilized to allow infusions from syringe pumps located outside the MRI scanning room. Once the application set was secured to the transcutaneous bone-anchored port, the infusions were initiated with 40 min linear ramps. The infusion rate was gradually increased to a maximum rate of 3 μL/min per catheter with a total volume of 600 μL of ^{64}Cu-NPs delivered per infusion. The inert aCSF is used to push the ^{64}Cu-NPs through the FVES, port, and catheters into the desired target. An additional dead volume is added to the overall volume to ensure only inert buffer is left within the implantable device between reaccess infusion periods. Once the infusion was finished, the catheters were left *in situ* for an additional 15 min, and the pump rate gradually decreased to stabilize the pressure before disconnecting the infusion lines. The application set was then removed from the port.

Positron Emission Tomography (PET). After attaching the infusion lines to the application set, the animal was positioned inside the brain coil for PET/MRI studies (Figure S21B). Emission data were collected over a 135 min period, beginning at the start of the infusion. To facilitate quantitative analysis and to study the biodistribution of ^{64}Cu-NPs at different time points, list-mode emission files were rebinned into nine frames of 15 min each to produce dynamic PET scans and reconstructed into a 256 × 256 × 89 matrix size (1.1718 mm × 1.1718 mm × 2.78 mm) using GE's Time of Flight Q.clear algorithm considering all quantitative corrections. Additionally, we acquired a single MRI scan in each session to serve as an anatomical guide for defining the Volume of Interest (VOI). The experimental timeline is shown in Figure S21C with detailed information provided in Supporting Information.

PET Data Analysis. Image analysis and visualization were carried out using GE's PET4D workstation, ImageJ, Amide v1.0.4 software, and MATLAB R2023a. PET data were analyzed in terms of line profiles (FWHM/FWTM), iso-contours, Vd, and TAC plots. Briefly, to assess FWHM/FWTM for each catheter, two lines perpendicular to the catheter trajectory were drawn on transverse and sagittal planes, and the final FWHM/FWTM was obtained by averaging the transverse and sagittal values. To assess iso-contours, three consecutive cross-sectional slices with the highest uptake value surrounding the left catheter from the same animal were averaged, normalized to the maximum value in the image, and then resampled to a finer grid of 1024×1024, and a contour plot was generated based on the processed image using an integrated program in MATLAB. The filled contour plot represents iso-lines obtained from an image and fills the areas between these iso-lines with consistent colors that correspond to the final image matrix values. For Vd analysis, an MRI-guided ellipsoidal VOI encompassing the entire brain was established for each scan, and Vd values were then computed by defining various threshold levels (ranging from 10% to 90% of the maximum uptake value within the VOI). Further, the activity inside the predefined VOIs at different time points was normalized to the total injected activity (A_{total}) to generate normalized TAC plots. It should be noted that for comparative analysis and statistical assessments among different groups of ^{64}Cu-NPs, AUC values were computed across all dynamically assessed plots. Detailed information regarding PET imaging and data analysis is provided in Supporting Information.

Statistical Analysis. Data were reported as mean values ± standard error of the mean (SEM), unless otherwise mentioned. Graphs were created in MATLAB 2023a. Statistical testing was performed using GraphPad Prism software version 5 (San Diego, CA, USA). One-way analysis of variance (ANOVA) followed by Tukey's test was selected to compare the AUC results (FWHM, TAC, and Vd) among different groups of ^{64}Cu-NPs with $p < 0.05$ considered significant. Significant difference was defined as $*p < 0.05$, $**p < 0.01$, $***p < 0.001$.

ASSOCIATED CONTENT

ⓈⅠ Supporting Information

The Supporting Information is available free of charge at https://pubs.acs.org/doi/10.1021/acsnano.4c04159.

Experimental procedures; analysis; experimental details of ^{64}Cu-DOTA-LIPs (Table S1); overview of ^{64}Cu-NPs prepared and supplied (Table S2); size exclusion and stability of ^{64}Cu-LIP(130) (Figure S1); radio-TLC of ^{64}Cu-LIP(130) (Figures S2−S4), ^{64}Cu-DOTA-TA complex (Figures S5−S7), ^{64}Cu-AuNP(40) (Figure S8), and ^{64}Cu-AuNP(8) (Figure S9); size exclusion, stability, and ICP-EOS characterization of ^{64}Cu-AuNPs (Figure S10); surface charge zeta potential measurements of ^{64}Cu-AuNP(40) and ^{64}Cu-AuNP(8) (Figure S11); UV−vis measurements of the ^{64}Cu-AuNP(40) and ^{64}Cu-AuNP-(8) (Figure S12); TEM of the ^{64}Cu-AuNP(40) and ^{64}Cu-AuNP(8) (Figure S13); neuroinfuse chronic drug delivery system (Figure S14); dynamic PET scans following ^{64}Cu-AuNP(40) (Figure S15), ^{64}Cu-AuNP(8) (Figure S16), and ^{64}Cu-LIP(130) (Figure S17); FWTM analysis and corresponding AUC plots (Figure S18); multi-threshold Vd calculation and corresponding AUC analysis (Figure S19); individual TAC and corresponding AUCs (Figure S20); experimental setup and infusion procedure (Figure S21) (PDF)

AUTHOR INFORMATION

Corresponding Authors

Mahsa Amirrashedi − *Department of Nuclear Medicine, Odense University Hospital, Odense 5000, Denmark; Department of Applied Mathematics and Computer Science, Technical University of Denmark, Lyngby 2800, Denmark; Danish Research Centre for Magnetic Resonance, Centre for Functional and Diagnostic Imaging and Research, Copenhagen University Hospital Amager and Hvidovre, Copenhagen 2650, Denmark;* ⓘ orcid.org/0009-0008-7466-8384; Email: maami@dtu.dk

Andreas Ingemann Jensen − *The Hevesy Laboratory, Department of Health Technology, Technical University of Denmark, Roskilde 4000, Denmark;* Email: atije@dtu.dk

Helge Thisgaard − *Department of Nuclear Medicine, Odense University Hospital, Odense 5000, Denmark; Department of Clinical Research and BRIDGE (Brain Research - Interdisciplinary Guided Excellence), University of Southern Denmark, Odense 5230, Denmark;* Email: helge.thisgaard@rsyd.dk

Bo Halle − *Department of Clinical Research and BRIDGE (Brain Research - Interdisciplinary Guided Excellence), University of Southern Denmark, Odense 5230, Denmark; Department of Neurosurgery, Odense University Hospital, Odense 5000, Denmark;* Email: bo.halle@rsyd.dk

Authors

Qing Tang − *The Hevesy Laboratory, Department of Health Technology, Technical University of Denmark, Roskilde 4000, Denmark*

Natan Johannes Willem Straathof − *The Hevesy Laboratory, Department of Health Technology, Technical University of Denmark, Roskilde 4000, Denmark*

Katharina Ravn − *The Hevesy Laboratory, Department of Health Technology, Technical University of Denmark, Roskilde 4000, Denmark*

Christian G.T. Pedersen − *Department of Nuclear Medicine, Odense University Hospital, Odense 5000, Denmark*

Louise Langhorn − *Biomedical Laboratory, University of Southern Denmark, Odense 5000, Denmark*

Frantz Rom Poulsen − *Department of Clinical Research and BRIDGE (Brain Research - Interdisciplinary Guided Excellence), University of Southern Denmark, Odense 5230, Denmark; Department of Neurosurgery, Odense University Hospital, Odense 5000, Denmark*

Max Woolley − *Renishaw Neuro Solutions Ltd (RNS), Gloucestershire GL12 8SP, United Kingdom*

David Johnson − *Renishaw Neuro Solutions Ltd (RNS), Gloucestershire GL12 8SP, United Kingdom*

Julia Williams − *Renishaw Neuro Solutions Ltd (RNS), Gloucestershire GL12 8SP, United Kingdom*

Charlotte Kidd − *Renishaw Neuro Solutions Ltd (RNS), Gloucestershire GL12 8SP, United Kingdom*

Complete contact information is available at:
https://pubs.acs.org/10.1021/acsnano.4c04159

Author Contributions

◆A.I.J., H.T., and B.H. contributed equally. A.I.J., H.T., and B.H. conceptualized the study. M.A., A.I.J., C.G.T.P., L.L., M.W.,

ABBREVIATIONS

BBB, blood−brain barrier; CED, convection-enhanced delivery; PEG, polyethylene glycol; NPs, nanoparticles; CNS, central nervous system; GBM, glioblastoma multiforme; ECM, extracellular matrix; Gd, gadolinium; MRI, magnetic resonance imaging; PET, positron emission tomography; ^{64}Cu-NPs, radiolabeled nanoparticles with copper-64; AuNPs, gold nanoparticles; LIPs, liposomes; $\varnothing_{vol\text{-}DLS}$, the volume-weighted hydrodynamic diameter measured by dynamic light scattering; $\varnothing_{TEM}$, the diameter of the AuNP gold core measured by transmission electron microscopy; PDI, polydispersity index; ζ, zeta potential; DLS, dynamic light scattering analysis; TEM, transmission electron microscopy; UV/vis, ultraviolet−visible spectroscopy; RCY, radiochemical yield; ndc, nondecay corrected; dc, decay corrected; RCC, radiochemical conversion; ICP−EOS, inductively coupled plasma−optical emission spectrometry; SEC, size-exclusion chromatography; ^{64}Cu-AuNP(8), radiolabeled gold nanoparticles with copper-64 and an average diameter of 8 nm; ^{64}Cu-AuNP(40), radiolabeled gold nanoparticles with copper-64 and an average diameter of 40 nm; ^{64}Cu-LIP(130), radiolabeled liposomes with copper-64 and an average diameter of 130 nm

REFERENCES

(1) Samal, J.; Rebelo, A. L.; Pandit, A. A Window into the Brain: Tools to Assess Pre-Clinical Efficacy of Biomaterials-Based Therapies on Central Nervous System Disorders. *Adv. Drug Delivery Rev.* **2019**, *148*, 68−145.

(2) Bobo, R. H.; Laske, D. W.; Akbasak, A.; Morrison, P. F.; Dedrick, R. L.; Oldfield, E. H. Convection-Enhanced Delivery of Macromolecules in the Brain. *Proc. Natl. Acad. Sci. U. S. A.* **1994**, *91*, 2076−2080.

(3) Groothuis, D. R. The Blood-Brain and Blood-Tumor Barriers: a Review of Strategies for Increasing Drug Delivery. *Neuro-Oncol.* **2000**, *2*, 45−59.

(4) Sampson, J. H.; Archer, G.; Pedain, C.; Wembacher-Schröder, E.; Westphal, M.; Kunwar, S.; Vogelbaum, M. A.; Coan, A.; Herndon, J. E.; Raghavan, R.; et al. Poor Drug Distribution As a Possible Explanation for the Results of the PRECISE Trial. *J. Neurosurg.* **2010**, *113*, 301−309.

(5) Allard, E.; Passirani, C.; Benoit, J. P. Convection-Enhanced Delivery of Nanocarriers for the Treatment of Brain Tumors. *Biomaterials* **2009**, *30*, 2302−2318.

(6) Halle, B.; Mongelard, K.; Poulsen, F. R. Convection-Enhanced Drug Delivery for Glioblastoma: A Systematic Review Focused on Methodological Differences in the Use of the Convection-Enhanced Delivery Method. *Asian J. Neurosurg.* **2019**, *14*, 5−14.

(7) Vecchio, D.; Daga, A.; Carra, E.; Marubbi, D.; Raso, A.; Mascelli, S.; Nozza, P.; Garrè, M. L.; Pitto, F.; Ravetti, J. L.; Vagge, S.; Corvò, R.; Profumo, A.; Baio, G.; Marcello, D.; Frosina, G. Pharmacokinetics, Pharmacodynamics and Efficacy on Pediatric Tumors of the Glioma Radiosensitizer KU60019. *Int. J. Cancer* **2015**, *136*, 1445−1457.

(8) Georgiou, C. J.; Cai, Z.; Alsaden, N.; Cho, H.; Behboudi, M.; Winnik, M. A.; Rutka, J. T.; Reilly, R. M. Treatment of Orthotopic U251 Human Glioblastoma Multiforme Tumors in NRG Mice by Convection-Enhanced Delivery of Gold Nanoparticles Labeled with the β-Particle-Emitting Radionuclide, (177)Lu. *Mol. Pharmaceutics* **2023**, *20*, 582−592.

(9) Inoue, T.; Yamashita, Y.; Nishihara, M.; Sugiyama, S.; Sonoda, Y.; Kumabe, T.; Yokoyama, M.; Tominaga, T. Therapeutic Efficacy of a Polymeric Micellar Doxorubicin Infused by Convection-Enhanced Delivery Against Intracranial 9L Brain Tumor Models. *Neuro-Oncol.* **2009**, *11*, 151−157.

(10) Gleason, J. M.; Klass, S. H.; Huang, P.; Ozawa, T.; Santos, R. A.; Fogarty, M. M.; Raleigh, D. R.; Berger, M. S.; Francis, M. B. Intrinsically Disordered Protein Micelles As Vehicles for Convection-Enhanced Drug Delivery to Glioblastoma Multiforme. *ACS Appl. Bio Mater.* **2022**, *5*, 3695−3702.

(11) Wu, G.; Barth, R. F.; Yang, W.; Kawabata, S.; Zhang, L.; Green-Church, K. Targeted Delivery of Methotrexate to Epidermal Growth Factor Receptor-Positive Brain Tumors by Means of Cetuximab (IMC-C225) Dendrimer Bioconjugates. *Mol. Cancer Ther.* **2006**, *5*, 52−59.

(12) Saito, R.; Krauze, M. T.; Bringas, J. R.; Noble, C.; McKnight, T. R.; Jackson, P.; Wendland, M. F.; Mamot, C.; Drummond, D. C.; Kirpotin, D. B.; Hong, K.; Berger, M. S.; Park, J. W.; Bankiewicz, K. S. Gadolinium-Loaded Liposomes Allow for Real-Time Magnetic Resonance Imaging of Convection-Enhanced Delivery in the Primate Brain. *Exp. Neurol.* **2005**, *196*, 381−389.

(13) MacKay, J. A.; Deen, D. F.; Szoka, F. C., Jr. Distribution in Brain of Liposomes After Convection Enhanced Delivery; Modulation by Particle Charge, Particle Diameter, and Presence of Steric Coating. *Brain Res.* **2005**, *1035*, 139−153.

(14) Mamot, C.; Nguyen, J. B.; Pourdehnad, M.; Hadaczek, P.; Saito, R.; Bringas, J. R.; Drummond, D. C.; Hong, K.; Kirpotin, D. B.; McKnight, T.; Berger, M. S.; Park, J. W.; Bankiewicz, K. S. Extensive Distribution of Liposomes in Rodent Brains and Brain Tumors Following Convection-Enhanced Delivery. *J. Neuro-Oncol.* **2004**, *68*, 1−9.

(15) Thorne, R. G.; Nicholson, C. In Vivo Diffusion Analysis with Quantum Dots and Dextrans Predicts the Width of Brain Extracellular Space. *Proc. Natl. Acad. Sci. U. S. A.* **2006**, *103*, 5567−5572.

(16) Hobbs, S. K.; Monsky, W. L.; Yuan, F.; Roberts, W. G.; Griffith, L.; Torchilin, V. P.; Jain, R. K. Regulation of Transport Pathways in Tumor Vessels: Role of Tumor Type and Microenvironment. *Proc. Natl. Acad. Sci. U. S. A.* **1998**, *95*, 4607−4612.

(17) Jensen, A. I.; Severin, G. W.; Hansen, A. E.; Fliedner, F. P.; Eliasen, R.; Parhamifar, L.; Kjær, A.; Andresen, T. L.; Henriksen, J. R. Remote-Loading of Liposomes with Manganese-52 and In Vivo Evaluation of the Stabilities of (52)Mn-DOTA and (64)Cu-DOTA Using Radiolabeled Liposomes and PET Imaging. *J. Controlled Release* **2018**, *269*, 100−109.

(18) Frellsen, A. F.; Hansen, A. E.; Jølck, R. I.; Kempen, P. J.; Severin, G. W.; Rasmussen, P. H.; Kjær, A.; Jensen, A. T.; Andresen, T. L. Mouse Positron Emission Tomography Study of the Biodistribution of Gold Nanoparticles with Different Surface Coatings Using Embedded Copper-64. *ACS Nano* **2016**, *10*, 9887−9898.

(19) Richardson, R. M.; Kells, A. P.; Rosenbluth, K. H.; Salegio, E. A.; Fiandaca, M. S.; Larson, P. S.; Starr, P. A.; Martin, A. J.; Lonser, R. R.; Federoff, H. J.; Forsayeth, J. R.; Bankiewicz, K. S. Interventional MRI-Guided Putaminal Delivery of AAV2-GDNF for a Planned Clinical Trial in Parkinson's Disease. *Mol. Ther.* **2011**, *19*, 1048−1057.

(20) Su, X.; Kells, A. P.; Salegio, E. A.; Richardson, R. M.; Hadaczek, P.; Beyer, J.; Bringas, J.; Pivirotto, P.; Forsayeth, J.; Bankiewicz, K. S. Real-Time MR Imaging with Gadoteridol Predicts Distribution of Transgenes After Convection-Enhanced Delivery of AAV2 Vectors. *Mol. Ther.* **2010**, *18*, 1490−1495.

(21) Christine, C. W.; Bankiewicz, K. S.; Van Laar, A. D.; Richardson, R. M.; Ravina, B.; Kells, A. P.; Boot, B.; Martin, A. J.; Nutt, J.; Thompson, M. E.; Larson, P. S. Magnetic Resonance Imaging-Guided Phase 1 Trial of Putaminal AADC Gene Therapy for Parkinson's Disease. *Ann. Neurol.* **2019**, *85*, 704−714.

(22) Stiles, D. Method to Determine Distribution of a Material by an Infused Magnetic Resonance Image Contrast Agent US 9,008,752 B2, 2015.

(23) Yao, Y.; Ding, X.; Qi, Y.; Qi, M.; Jones, A. Using MRI to Determine Gadolinium Contrast Agent Concentration in Convection-Enhanced Delivery. *Brain Tumor Res. Treat* **2022**, *10*, S60−1.

(24) Salegio, E. A.; Cukrov, M.; Lortz, R.; Green, A.; Lambert, E.; Copeland, S.; Gonzalez, M.; Stockinger, D. E.; Yeung, J. M.; Hwa, G. G. C. Feasibility of Targeted Delivery of AAV5-GFP into the Cerebellum of Nonhuman Primates Following a Single Convection-Enhanced Delivery Infusion. *Hum. Gene Ther.* **2022**, *33*, 86−93.

(25) Spinazzi, E. F.; Argenziano, M. G.; Upadhyayula, P. S.; Banu, M. A.; Neira, J. A.; Higgins, D. M. O.; Wu, P. B.; Pereira, B.; Mahajan, A.; Humala, N.; et al. Chronic Convection-Enhanced Delivery of Topotecan for Patients with Recurrent Glioblastoma: a First-In-Patient, Single-Centre, Single-Arm, Phase 1b Trial. *Lancet Oncol.* **2022**, *23*, 1409−1418.

(26) Salegio, E. A.; Campagna, M. V.; Allen, P. C.; Stockinger, D. E.; Song, Y.; Hwa, G. G. Targeted Delivery and Tolerability of MRI-Guided CED Infusion into the Cerebellum of Nonhuman Primates. *Hum. Gene Ther: Methods* **2018**, *29*, 169−176.

(27) Jensen, A. T.; Binderup, T.; Andresen, T. L.; Kjær, A.; Rasmussen, P. H. PET Imaging of Liposomes Labeled with an [^{18}F]-Fluorocholesteryl Ether Probe Prepared by Automated Radiosynthesis. *J. Liposome Res.* **2012**, *22*, 295−305.

(28) Lilius, T. O.; Mortensen, K. N.; Deville, C.; Lohela, T. J.; Stæger, F. F.; Sigurdsson, B.; Fiordaliso, E. M.; Rosenholm, M.; Kamphuis, C.; Beekman, F. J.; et al. Glymphatic-Assisted Perivascular Brain Delivery of Intrathecal Small Gold Nanoparticles. *J. Controlled Release* **2023**, *355*, 135−148.

(29) Sporer, E.; Poulie, C. B.; Lindegren, S.; Aneheim, E.; Jensen, H.; Bäck, T.; Kempen, P. J.; Kjaer, A.; Herth, M. M.; Jensen, A. I. Surface Adsorption of the Alpha-Emitter Astatine-211 To Gold Nanoparticles Is Stable In Vivo and Potentially Useful in Radionuclide Therapy. *J. Nanotheranostics* **2021**, *2*, 196−207.

(30) Mozafari, M.; Mazaheri, E.; Dormiani, K. Simple Equations Pertaining to the Particle Number and Surface Area of Metallic, Polymeric, Lipidic and Vesicular Nanocarriers. *Sci. Pharm.* **2021**, *89*, 15.

(31) Healy, A. T.; Vogelbaum, M. A. Convection-Enhanced Drug Delivery for Gliomas. *Surg. Neurol. Int.* **2015**, *6*, S59.

(32) Wang, Y.; Jiang, Y.; Wei, D.; Singh, P.; Yu, Y.; Lee, T.; Zhang, L.; Mandl, H. K.; Piotrowski-Daspit, A. S.; Chen, X.; et al. Nanoparticle-Mediated Convection-Enhanced Delivery of a DNA Intercalator to Gliomas Circumvents Temozolomide Resistance. *Nat. Biomed. Eng.* **2021**, *5*, 1048−1058.

(33) Stephen, Z. R.; Chiarelli, P. A.; Revia, R. A.; Wang, K.; Kievit, F.; Dayringer, C.; Jeon, M.; Ellenbogen, R.; Zhang, M. Time-Resolved MRI Assessment of Convection-Enhanced Delivery by Targeted and Nontargeted Nanoparticles in a Human Glioblastoma Mouse Model. *Cancer Res.* **2019**, *79*, 4776−4786.

(34) Finbloom, J. A.; Aanei, I. L.; Bernard, J. M.; Klass, S. H.; Elledge, S. K.; Han, K.; Ozawa, T.; Nicolaides, T. P.; Berger, M. S.; Francis, M. B. Evaluation of Three Morphologically Distinct Virus-Like Particles As Nanocarriers for Convection-Enhanced Drug Delivery to Glioblastoma. *Nanomaterials* **2018**, *8*, 1007.

(35) Josowitz, A. D.; Bindra, R. S.; Saltzman, W. M. Polymer Nanocarriers for Targeted Local Delivery of Agents in Treating Brain Tumors. *Nanotechnology* **2023**, *34*, 072001.

(36) Zhou, J.; Patel, T. R.; Sirianni, R. W.; Strohbehn, G.; Zheng, M. Q.; Duong, N.; Schafbauer, T.; Huttner, A. J.; Huang, Y.; Carson, R. E.; et al. Highly Penetrative, Drug-Loaded Nanocarriers Improve Treatment of Glioblastoma. *Proc. Natl. Acad. Sci. U. S. A.* **2013**, *110*, 11751−11756.

(37) Phillips, W. T.; Bao, A.; Brenner, A. J.; Goins, B. A. Image-Guided Interventional Therapy for Cancer with Radiotherapeutic Nanoparticles. *Adv. Drug Delivery Rev.* **2014**, *76*, 39−59.

(38) Saito, R.; Bringas, J. R.; McKnight, T. R.; Wendland, M. F.; Mamot, C.; Drummond, D. C.; Kirpotin, D. B.; Park, J. W.; Berger, M. S.; Bankiewicz, K. S. Distribution of Liposomes into Brain and Rat Brain Tumor Models by Convection-Enhanced Delivery Monitored with Magnetic Resonance Imaging. *Cancer Res.* **2004**, *64*, 2572−2579.

(39) Nance, E. A.; Woodworth, G. F.; Sailor, K. A.; Shih, T. Y.; Xu, Q.; Swaminathan, G.; Xiang, D.; Eberhart, C.; Hanes, J. A Dense Poly(Ethylene Glycol) Coating Improves Penetration of Large Polymeric Nanoparticles within Brain Tissue. *Sci. Transl. Med.* **2012**, *4*, 149ra119.

(40) Birzu, C.; French, P.; Caccese, M.; Cerretti, G.; Idbaih, A.; Zagonel, V.; Lombardi, G. Recurrent Glioblastoma: From Molecular Landscape to New Treatment Perspectives. *Cancers* **2021**, *13*, 47.

(41) Saito, R.; Krauze, M. T.; Noble, C. O.; Tamas, M.; Drummond, D. C.; Kirpotin, D. B.; Berger, M. S.; Park, J. W.; Bankiewicz, K. S. Tissue Affinity of the Infusate Affects the Distribution Volume During Convection-Enhanced Delivery into Rodent Brains: Implications for Local Drug Delivery. *J. Neurosci. Methods* **2006**, *154*, 225−232.

(42) Saucier-Sawyer, J. K.; Seo, Y. E.; Gaudin, A.; Quijano, E.; Song, E.; Sawyer, A. J.; Deng, Y.; Huttner, A.; Saltzman, W. M. Distribution of Polymer Nanoparticles by Convection-Enhanced Delivery to Brain Tumors. *J. Controlled Release* **2016**, *232*, 103−112.

(43) Sonabend, A. M.; Stuart, R. M.; Yun, J.; Yanagihara, T.; Mohajed, H.; Dashnaw, S.; Bruce, S. S.; Brown, T.; Romanov, A.; Sebastian, M.; et al. Prolonged Intracerebral Convection-Enhanced Delivery of Topotecan with a Subcutaneously Implantable Infusion Pump. *Neuro-Oncol.* **2011**, *13*, 886−893.

(44) Lonser, R. R.; Warren, K. E.; Butman, J. A.; Quezado, Z.; Robison, R. A.; Walbridge, S.; Schiffman, R.; Merrill, M.; Walker, M. L.; Park, D. M.; et al. Real-Time Image-Guided Direct Convective Perfusion of Intrinsic Brainstem Lesions. *J. Neurosurg.* **2007**, *107*, 190−197.

(45) Iyer, R. R.; Butman, J. A.; Walbridge, S.; Gai, N. D.; Heiss, J. D.; Lonser, R. R. Tracking Accuracy of T2- and Diffusion-Weighted Magnetic Resonance Imaging for Infusate Distribution by Convection-Enhanced Delivery. *J. Neurosurg.* **2011**, *115*, 474−480.

(46) Boschi, A.; Martini, P.; Janevik-Ivanovska, E.; Duatti, A. The Emerging Role of Copper-64 Radiopharmaceuticals as Cancer Theranostics. *Drug Discovery Today* **2018**, *23*, 1489−1501.

(47) Anderson, C. J.; Ferdani, R. Copper-64 Radiopharmaceuticals for PET Imaging of Cancer: Advances in Preclinical and Clinical Research. *Cancer Biother.Radiopharm.* **2009**, *24*, 379−393.

(48) Boucher, Y.; Baxter, L. T.; Jain, R. K. Interstitial Pressure Gradients in Tissue-Isolated and Subcutaneous Tumors: Implications for Therapy. *Cancer Res* **1990**, *50*, 4478−4484.

(49) Yang, Y.; Zhan, W. Role of Tissue Hydraulic Permeability in Convection-Enhanced Delivery of Nanoparticle-Encapsulated Chemotherapy Drugs to Brain Tumour. *Pharm. Res.* **2022**, *39*, 877−892.

(50) Morrison, P. F.; Chen, M. Y.; Chadwick, R. S.; Lonser, R. R.; Oldfield, E. H. Focal Delivery During Direct Infusion to Brain: Role of

Flow Rate, Catheter Diameter, and Tissue Mechanics. *Am. J. Physiol. Regul. Integr. Comp. Physiol.* **1999**, *277*, R1218−1229.

(51) Bauman, M.; Gillies, G.; Raghavan, R.; Brady, M.; Pedain, C. Physical Characterization of Neurocatheter Performance in a Brain Phantom Gelatin with Nanoscale Porosity: Steady-State and Oscillatory Flows. *Nanotechnology* **2004**, *15*, 92.

(52) Chen, M. Y.; Lonser, R. R.; Morrison, P. F.; Governale, L. S.; Oldfield, E. H. Variables Affecting Convection-Enhanced Delivery to the Striatum: A Systematic Examination of Rate of Infusion, Cannula Size, Infusate Concentration, and Tissue-Cannula Sealing Time. *J. Neurosurg.* **1999**, *90*, 315−320.

(53) Sampson, J. H.; Brady, M. L.; Petry, N. A.; Croteau, D.; Friedman, A. H.; Friedman, H. S.; Wong, T.; Bigner, D. D.; Pastan, I.; Puri, R. K.; et al. Intracerebral Infusate Distribution by Convection-Enhanced Delivery in Humans with Malignant Gliomas: Descriptive Effects of Target Anatomy and Catheter Positioning. *Oper. Neurosurg.* **2007**, *60*, 89−98.

(54) Lewis, O.; Woolley, M.; Johnson, D. E.; Fletcher, J.; Fenech, J.; Pietrzyk, M. W.; Barua, N. U.; Bienemann, A. S.; Singleton, W.; Evans, S. L.; et al. Maximising Coverage of Brain Structures Using Controlled Reflux, Convection-Enhanced Delivery and the Recessed Step Catheter. *J. Neurosci. Methods* **2018**, *308*, 337−345.

(55) Sager, T. M.; Castranova, V. Surface Area of Particle Administered Versus Mass in Determining the Pulmonary Toxicity of Ultrafine and Fine Carbon Black: Comparison to Ultrafine Titanium Dioxide. *Part. Fibre Toxicol.* **2009**, *6*, 15.

(56) Senut, M. C.; Zhang, Y.; Liu, F.; Sen, A.; Ruden, D. M.; Mao, G. Size-Dependent Toxicity of Gold Nanoparticles on Human Embryonic Stem Cells and Their Neural Derivatives. *Small* **2016**, *12*, 631−646.

(57) Ninik, Ł.; Noga, M.; Kobylarz, D.; Frydrych, A.; Króniak, A.; Kapka-Skrzypczak, L.; Jurowski, K. Gold Nanoparticles (AuNPs)—Toxicity, Safety and Green Synthesis: A Critical Review. *Int. J. Mol. Sci.* **2024**, *25*, 4057.

(58) Bailly, A.-L.; Correard, F.; Popov, A.; Tselikov, G.; Chaspoul, F.; Appay, R.; Al-Kattan, A.; Kabashin, A. V.; Braguer, D.; Esteve, M.-A. In Vivo Evaluation of Safety, Biodistribution and Pharmacokinetics of Laser-Synthesized Gold Nanoparticles. *Sci. Rep.* **2019**, *9*, 12890.

(59) Bienemann, A.; White, E.; Woolley, M.; Castrique, E.; Johnson, D. E.; Wyatt, M.; Murray, G.; Taylor, H.; Barua, N.; Gill, S. S. The Development of an Implantable Catheter System for Chronic or Intermittent Convection-Enhanced Delivery. *J. Neurosci. Methods* **2012**, *203*, 284−291.

(60) White, E.; Woolley, M.; Bienemann, A.; Johnson, D. E.; Wyatt, M.; Murray, G.; Taylor, H.; Gill, S. S. A Robust MRI-Compatible System to Facilitate Highly Accurate Stereotactic Administration of Therapeutic Agents to Targets within the Brain of a Large Animal Model. *J. Neurosci. Methods-* **2011**, *195*, 78−87.

(61) Barua, N.; Woolley, M.; Bienemann, A.; Johnson, D.; Lewis, O.; Wyatt, M.; Irving, C.; O'Sullivan, S.; Murray, G.; Fennelly, C.; et al. Intermittent Convection-Enhanced Delivery to the Brain Through a Novel Transcutaneous Bone-Anchored Port. *J. Neurosci. Methods* **2013**, *214*, 223−232.